الآية

قال تعالى:"وَعَلَّمَ آدَمَ الْأَسْمَاءَ كُلَّهَا ثُمَّ عَرَضَهُمْ عَلَى الْمَلَائِكَةِ فَقَالَ أَنْبِئُونِي بِأَسْمَاءِ هَؤُلَاءِ إِنْ كُنْتُمْ صَادِقِينَ (31) قَالُوا سُبْحَانَكَ لَا عِلْمَ لَنَا إِلَّا مَا عَلَّمْتَنَا إِنَّكَ أَنْتَ الْعَلِيمُ الْحَكِيمُ (32)"

صدق الله العظيم

سورة البقرة الآيه(31_32)

Dedication

To my family

My teachers

And my friends

Acknowledgements

Firstly, *great praise and thanks be to Allah for completion of this study.*

Secondly, *my thanks and respect to Dr. Ahmed Abukonna who support me and gave me confidence and this time.*

Finally, I *would like to express my thanks to all teachers.*

Abstract

The renal sinus is a space that forms the medial border of the kidney and is surrounded by the renal parenchyma laterally. The renal arteries, veins, lymphatic vessels, nerve fibers, renal pelvis and major and minor calices are located within the renal sinus. 50 images were used in the study. The study conducted at radiology department in Royal Care hospital using CT scan 64 slice manufactured by Toshiba. Then the image were read by IDL in TIFF format and the user clicks on areas represents the renal cortex, renal sinus fat and psoas muscle fat area in case of test group; in these areas a window 3×3 pixel were generated and textural feature for the classes center were generated. These textural features includes FOS; (coefficient of variation, stander deviation, variance, signal, energy, and entropy) were used. These features were assigned as classification center using the Euclidian distances to classify the whole image.

The result of the study revealed that the classification accuracy result using linear discriminant function, in which 93.4% of original grouped cases correctly classified. Overall classification accuracy = 93.4%. Sensitivity of renal sinus, kidney tissue and abdominal fat = 87.7%, 100%, and 94.0% respectively. In respect to the applied features the mean, SD, energy and entropy on CT images can differentiate between renal sinus fat and rest of the tissue successfully and the best feature is the mean followed by energy, then entropy and the least is SD.

Texture analysis depending on the relative attenuation coefficient of tissues could serve the diagnostic field and overcoming the visual diagnosis that comes with different interpretation.

ملخص البحث

الجيب الكلوي هو الفراغ الذي يشكل الحدود الداخلية من الكلى وتحيط بها النسيج الكلوي أفقيا. الشرايين الكلوية، الأوردة، الأوعية اللمفاوية، الألياف العصبية تقع داخل الجيوب الكلوية. تم استخدام 50 صورة في الدراسة و التي أجريت في قسم الأشعة في مستشفى رويال كير باستخدام الأشعة المقطعية ذات 64 شريحة المصنعة من قبل توشيبا. ثم تم قراءة الصورة ببرنامج (IDL) على مناطق تمثل القشرة الكلوية، دهون الجيب الكلوي و دهون عضلات البطن. في هذه المناطق تم إنشاء نافذة 3 × 3 وتم إنشاء الميزة التكوينية لمركز الطبقات. وتشمل هذه الملامح التكوينية.(معامل الاختلاف، الانحراف المعياري، التباين، الإشارة، الطاقة، والانتظام). تم تعيين هذه الميزات كمركز تصنيف باستخدام المسافات لتصنيف الصورة بأكملها.

وكشفت نتائج الدراسة أن نتيجة دقة التصنيف باستخدام الدالة التمييزية الخطية، حيث تم تصنيف 93.4٪ من الحالات الأصلية بشكل صحيح. دقة التصنيف الإجمالية = 93.4٪. حساسية الجيب الكلوي، أنسجة الكلى والدهون في البطن = 87.7٪، 100٪، و 94.0٪ على التوالي. فيما يتعلق بالميزات التطبيقية التي يمكن أن تفرق في الصور بين دهون جيب الكلوية ودهون عضلة البطن من الأنسجة بنجاح. وأفضل ميزة هوالوسط الحسابي تليها الطاقة، ثم درجة الانتظام والأقل هوالانحراف المعياري.

تحليل النسيج اعتمادا على معامل التوهين النسبي للأنسجة يمكن أن يخدم المجال التشخيصي والتغلب على التشخيص البصري الذي يأتي مع تفسير مختلف.

List of contact

List of Table

List of figures:

List of Abbreviations

CT Computed Tomography
EPA Environmental protection agency

DHA Docosahexaenoic acid

HU Hounsfield unit
Lt RSF Left renal sinus fat
RT RSF Right renal sinus fat

IDL Interactive data language

Chapter one

Introduction

1.1 Introduction:

The renal sinus (RS) is a space that forms the medial border of the kidney and is surrounded by the renal parenchyma laterally. The renal arteries, veins, lymphatic vessels, nerve fibers, renal pelvis and major and minor calices are located within the RS. Properly functioning kidneys are essential for maintaining proper blood volume and composition; for filtering and excreting or saving various chemical metabolites; and for helping to maintain proper blood pressure. Hypertension (high blood pressure) is known to result from improperly functioning kidneys. Research carried out during the last few years indicates that both saturated fat and cholesterol play important roles in maintaining kidney function, as do the omega-3 fatty acids(Sokhi et al., 2015).

The kidneys need stable fats both for their cushioning and as their energy source. We know that the kidney fat normally has a higher concentration of the important saturated fatty acids than are found in any of the other fat depots. These saturated fatty acids are myristic acid (the 14-carbon saturate), palmitic acid (the 16-carbon saturate), and stearic acid (the 18-carbon saturate). When we consume various polyunsaturated fatty acids in large amounts, they are incorporated into kidney tissues, usually at the expense of oleic acid, because the normal high level of saturated fatty acids in the kidney fat does not change(Murakami et al., 2016).

A species of rat known to be prone to strokes and to spontaneously develop hypertension (high blood pressure) has been used to evaluate effects of

different lipids such as plant sterols or cholesterol, and also fatty acids such as omega-3 or omega-6 fatty acids in the finely tuned functions of the kidney. These animals are very sensitive to dietary cholesterol manipulations and a deficiency of cholesterol in their membranes makes their membranes weak and fragile. When plant sterols found in vegetable oils are substituted for cholesterol in their diets, these animals have a shortened life span. Also, these animals are reported to need a proper omega-6 to omega-3 ratio in the kidney phospholipids (Dwyer et al., 1995).

The observation of renal sinus fat is important for detecting a small tumor location in that area and determining the exact tumor stage. Multiplaner CT or MR images can allow exact evaluation of extend of complex renal sinus diseases. CT is the most sensitive, effective, comprehensive image modality for evaluating the kidney and for a wide variety of renal sinus lesion, multicolimater CT provide faster scan and image acquisition and improve spatial resolution by using thinner collimation, multiplanner reconstruction image can allows exact determination of the extent of complex renal sinus diseases, the coronal plane is the most useful for the evaluation of renal sinus lesion because it provide comprehensive view of kidney, including renal sinus.

The computer programs like IDL was been used to analysis the image data from CT, to improve the image, and analysis the image data. IDL is computer software system, is an acronym for interactive data language, consist of both interactive programing environment and program language, its used wide range of science and engineering discipline for processing and analyzing numerical image data.

While obesity as defined based on body mass index (BMI) is associated with the development of CKD, reports indicate that measures of abdominal adiposity are also associated with CKD(Montani et al., 2004). The observed associations of abdominal adiposity with CKD suggest that regional fat accumulation and ectopic fat, defined as the accumulation of fat within and around non-adipose tissues and organs, may mediate the relation of obesity to renal function(Dietrich and Kangarloo, 1986). Within the kidney, ectopic fat can accumulate within the renal sinus, a renal cavity that also contains the renal artery, renal vein, lymphatic vessels, and nerves and has been observed in humans and in an animal model of diet-induced obesity (Dwyer et al., 1995). It is hypothesized to impair renal function through compression of renal structures, the release of locally acting molecules, or lipotoxicity in renal tissue (Vora et al., 2017).

Because the effects of such organ-specific fat accumulation are not captured using traditional anthropometric measurements of adiposity, radiographic techniques are necessary to investigate the potential role of kidney-specific fat accumulation in renal function.

1.2Problem of the study:

Renal sinus fat may obesity-related vascular disease, and other health issue, the computer programs allow to identify the different between the sinus fat tissues and renal tissue to give accurate results for the amount of fat tissue in the renal sinus to renal tissue, and calculation of the fat volume by using image processing techniques.

1.3 Objectives of the study

1.3.1 General objectives:

The main objective of this study was to characterize the renal sinus fat in CT images using texture analysis.

1.3.2 Specific objectives:

- To identify the different between abdominal fat tissue and renal tissue by the differences in density of each one of them.
- To measure the amount of fat tissue inside the renal.

1.4 Overview of the study:

This study consist of five chapters, with chapter one as an introduction , problem of the study, objectives, significance of the study and the overview as end of this chapter) ,Followed by chapter two which include :(anatomy, physiology, basics of texture analysis), a literature review that includes a comprehensive review of the scholarly literature. The material and method will be cited in chapter three while Chapter four includes result presentation and finally chapter five includes :(discussion, conclusion, and recommendations).

Chapter Two

Literature review

2.1 Anatomy of the urinary system

2.1.1. The kidneys:

The kidneys are reddish brown and lie behind the peritoneum and the posterior abdominal wall on either side of vertebral column. Each kidney is 12cm in length, 5cm in wide 2.5cm in thick. It has convex lateral surface and concave medial surface [through which the renal vessels, the lymphatic and the ureter pass] also has an anterior and posterior surface and an upper and lower pole. On the medial surface of the kidney there is hilum which leads to renal sinus. The sinus contains major and minor calyces which the expansion of them and upper ureter made the renal pelvis(Patton, 2015).

The kidneys have the following coverings; Fibrous capsule: this surrounds the kidney and is closely applied to its outer surface. Perirenal fat: this cover the fibrous capsule. Renal fascia: this condensation of connective tissue that lies outside the perirenal fat and encloses the kidneys and suprarenal gland, it's continuous laterally with the fascia transversals. Para renal fat: this lies external to renal fascia and its form part of the retroperitoneal fat. All this coverings support the kidneys and hold them on the posterior abdominal wall(Patton, 2015).

2.1.1.2 Structure of the kidneys:

The kidney consist of reddish brown outer part the cortex , and paler inner portion ,the medulla which composed of pyramids .The pyramids contain the collecting tubule which open on the papillae and this project into minor

calyces. The essential functional unit of kidney is nephron and there one million of them on each adult kidney .The nephron consist of renal corpuscle, tubule and associated blood vessels(Tarzamni et al., 2016).

2.1.1.3 The relations of kidneys:

Right kidney: Anteriorly: The suprarenal gland, the liver, the second part of duodenum, and the right colic flexure. Posteriorly: The diaphragm; the cost diaphragmatic recess of the pleura; the 12^{th} rib; and the psoas, quadrateslumbrum, and transverse abdominis muscles, and ilioinguinal nerves run downward and laterally.

Left kidney: Anteriorly: the suprarenal gland, the spleen, the stomach, the pancreases, the left colic flexure, and coils of jejunum. Posteriorly: the diaphragm; the cost diaphragmatic recess of the pleura; the 11^{th} and 12^{th} rips; and the psoas, quadrates lumbered, and transverse abdominal muscle, and ilioguinal nerves run downward and laterally(Tarzamni et al., 2016).

2.1.1.4Blood Supply:

Arteries: The renal artery arises from the aorta at the level of the second lumbar vertebra. Renal artery divides into five segmental arteries that enter the hilum of the kidney. Lobar arteries arise from each segmental artery, each lobar gives off two or three interloper arteries. The interloper arteries run toward the cortex on each side of renal pyramid. At the junction of the cortex and medulla the interloper arteries give off the accurate arteries. The accurate arteries give of several interlobular arteries that ascend in the cortex. Then the interlobular arteries branches into afferent glomerular arterioles.

Veins: the renal vein emerges from the hilum in front of the renal artery and drain in to the inferior vena cava(Tarzamni et al., 2016).

Lymph drainage**:** lymph drains to the lateral aortic lymph nodes around the origin of the renal artery. Nerve supply: the nerve supply is the renal sympathetic plexus.

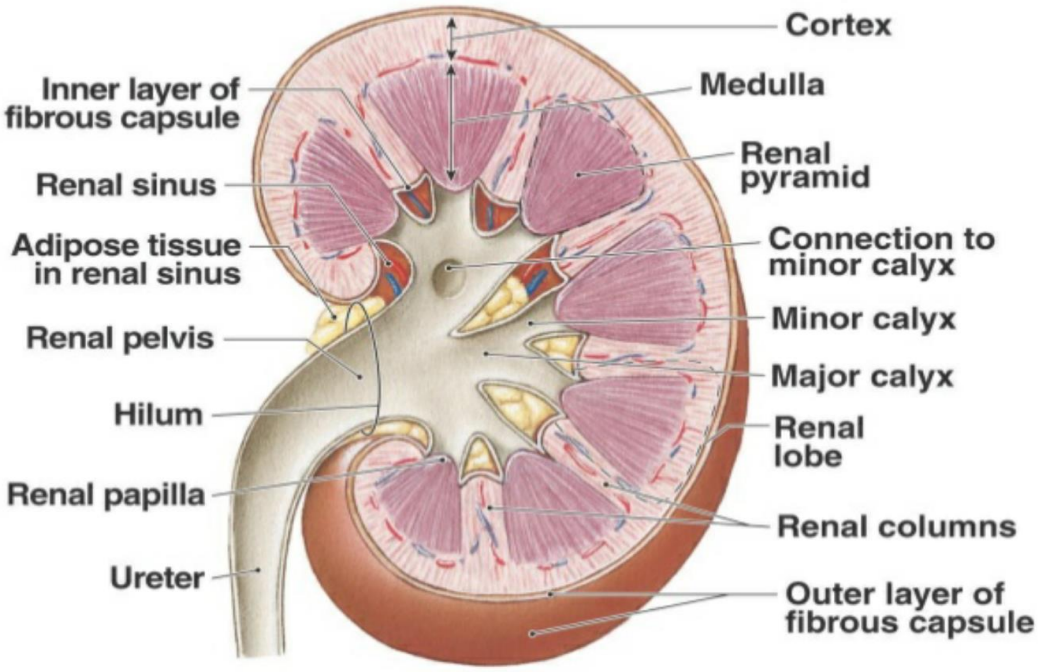

Figure 2.2. Show anatomy of the kidney.

2.2. Physiology of the urinary system:

2.2.1The kidney:

The kidney playas major role in the control of the constancy of the internal environment. The blood flowing in the kidneys is first filtered by glomerular filtration, so that all blood constituents except blood cell and plasma proteins go in to micro tubular system. In the tubules the useful substance including the filtered water, glucose and protein are quickly reabsorbed (tubular

reabsorption) back into the blood. Unwanted substances that escape filtration are quickly secreted into tubular lumen (tubular section). There are several hormones (antidiuretic hormone and aldosterone) act on the kidney to enable it to adjust the final composition of urine. The glomerular filtrate flows first into proximal convoluted tubules which absorbed useful substances and then the filtrate passes into the descending limb of loop of the henle which play major role in the urine concentration. The ascending limb of the loop is joins to the distal convoluted tubules and the latter is joining to the collecting duct. The urine from the collecting duct go to renal papillae which open in to minor calyces of renal pelvis and then pass through major calyces to renal pelvis(Patton, 2015).

2.2.2. The ureter:

The urine from the renal pelvis convey to the urinary bladder by the ureter.

2.2.3. The urinary bladder:

The urinary bladder store the urine and voided at intervals by process act of micturition which consist of contraction of muscles of bladder and relaxation of sphincter of urethra and the then urine flow throughout the body by urethra.

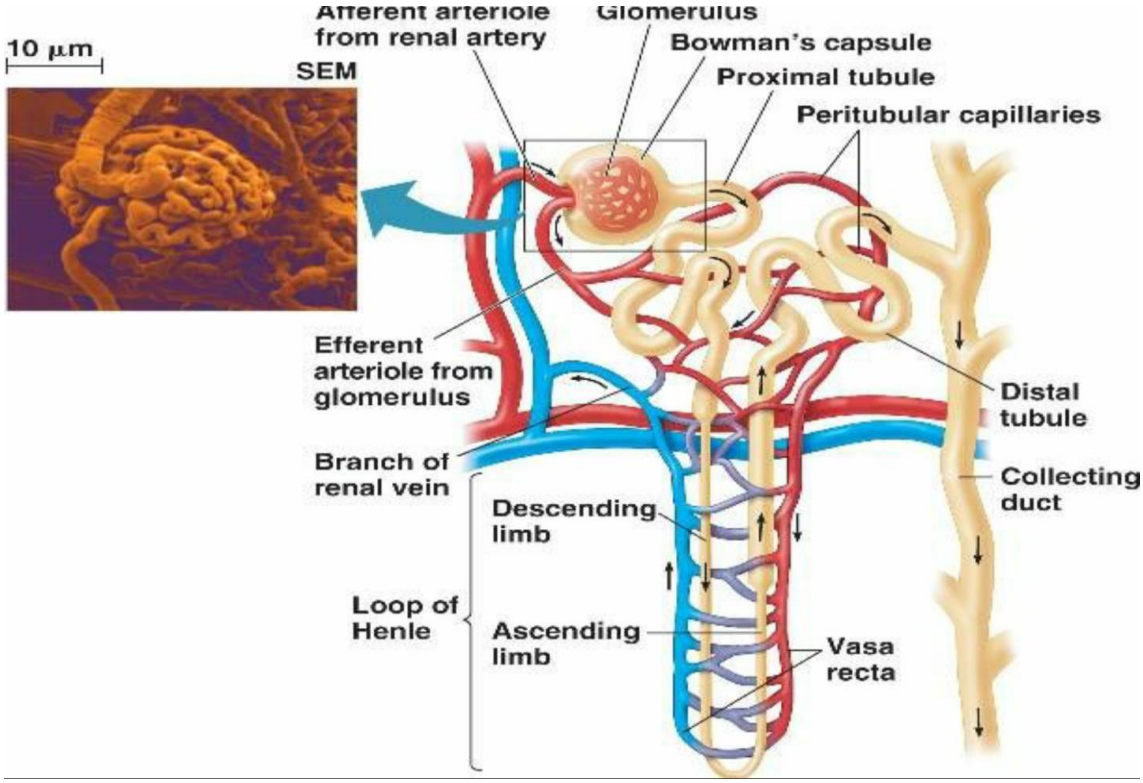

Figure2.3. Show the nephrons

2.3 Texture Analysis Methods in Biomedical Image Processing:

Imaging physics as a developed field of study provide different diagnosis tools for different researchers such as clinicians and biologists. Popular imaging modalities are X-ray, Computed Tomography (CT) and Magnetic Resonance Imaging (MRI), 3-Dultrasound and whole slide microscopy images which widely used in clinical routine for different aims. For example, MRI imaging is a common and powerful approach to represent the soft tissues of the human body, which can be used for three-dimensional visualization of the body organs (Ahmadvand and Daliri, 2015).

Extraction of target tissues, tumors and lesions like MS are the preliminary step in many medical procedures. For instance, extraction of three main cerebral tissues such as white matter, gray matter and cerebrospinal fluid is

an important step for different diagnosis and treatment procedures such as 3D-brain visualization, heterotopia, and brain atrophy (Ahmadvand et al., 2015a). Currently, computerized analysis of image data has become one of the main subjects in diagnostic procedures. This important field of research area is known as computer-aided diagnosis (CAD). These methods mainly provide a description of pathologic tissues for radiologists, biologist and, so forth for detection and diagnosis of normal and pathological tissues (Ojala et al., 2001). Textures are one of the vital features in image processing and especially biomedical image analysis. Although, textures look intuitive, so far a single unifying of them have not been suggested, which could present a comprehensive definition for textures. Therefore, researchers proposed different methods for extraction of texture features, which each group of features have their positive and negative properties as well. Textures as an important property in medical images have attracted much attention in CAD systems. Texture analysis methods can be divided in different sub-categories(Depeursinge et al., 2014).

2.3.1 Statistical Methods:

Statistical features consist of different categories such as first-order, second-order statistical methods, Local Binary Pattern (LBP) methods and so forth. These features especially LBP have been the center of attention because of obtaining promising results which they recently have achieved in different applications with changing in level of noises, illumination, sizes of textures. As medical images are detected by many artifacts during imaging providing an invariant group of features is crucial in these applications(Haralick and Shanmugam, 1973).

2.3.1.1 First order and second order methods:

The first order statistical features include the features which are extracted from the statistical property of image histogram including mean, variance, standard deviation and etc. Although these features are very straightforward and simple, they provide a good description of texture in the image. Moreover, there are three main sub-categories which have been proposed for second-order statistical features including Spatial Grey-level difference Method based on the analysis of co-occurrence matrix, the Grey-Level difference and the Grey-Level Run Method. Statistical features have widely been used for extraction of relevant features in CAD systems(Karahaliou et al., 2007).

The first-order histogram P (I) is defined as:

$$P(I) = \frac{\text{number of pixels with gray level } I}{\text{total number of pixels in the region}}$$

Based on the definition of P (I), the Mean $m_1$and Central Moments μkof Iare given by:

$$m_1 = E\left[I^1\right] = \sum_{I=0}^{N_g-1} I^1 P(I)$$

$$\mu_k = E\left[\left(I - E\left[I\right]\right)^k\right] = \sum_{I=0}^{N_g-1} (I - m_1)^k P(I),$$

$$k = 2, 3, 4$$

Where Ngis the number of possible gray levels. The most frequently used central moments are Variance, Skewness and Kurtosis given by μ2, μ3, and μ4 respectively. The Variance is a measure of the histogram width that

measures the deviation of gray levels from the Mean. Skewness is a measure of the degree of histogram asymmetry around the Mean and Kurtosis is a measure of the histogram sharpness.

The histogram of intensity levels is obviously a concise and simple summary of the statistical information contained in the image. Calculation of the grey-level histogram involves single pixels. Thus the histogram contains the first-order statistical information about the image (or its fragment). Dividing the values h(i) by the total number of pixels in the image one obtains the approximate probability density of occurrence of the intensity levels.

$$p(i) = h(i) / NM , \qquad i = 0,1,\ldots,G\text{-}1$$

The histogram can be easily computed, given the image. The shape of the histogram provides many clues as to the character of the image. For example, a narrowly distributed histogram indicated the low-contrast image. A bimodal histogram often suggests that the image contained an object with a narrow intensity range against a background of differing intensity. Different useful parameters (image features) can be worked out from the histogram to quantitatively describe the first-order statistical properties of the image. Most often the so-called central moments (Papoulis 1965) are derived from it to characterize the texture, as defined by Equations below

Mean: $$\mu = \sum_{i=0}^{G-1} ip(i)$$

Variance: $$\sigma^2 = \sum_{i=0}^{G-1} (i-\mu)^2 p(i)$$

Skewness: $$\mu_3 = \sigma^{-3} \sum_{i=0}^{G-1} (i-\mu)^3 p(i)$$

Kurtosis: $$\mu_4 = \sigma^{-4} \sum_{i=0}^{G-1} (i-\mu)^4 p(i) - 3$$

The features generated from the first-order statistics provide information related to the gray-level distribution of the image. However they do not give any information about the relative positions of the various gray levels within the image. These features will not be able to measure whether all low-value gray levels are positioned together, or they are interchanged with the high-value gray levels. An occurrence of some gray-level configuration can be described by a matrix of relative frequencies $P_{\theta,d}(I_1, I_2)$. It describes how frequently two pixels with gray-levels I_1,I_2appear in the window separated by a distance din direction θ. The information can be extracted from the co-occurrence matrix that measures second-order image statistics, where the pixels are considered in pairs. The co-occurrence matrix is a function of two parameters: relative distance measured in pixel numbers (d) and their relative orientation θ. The orientation θ is quantized in four directions that represent horizontal, diagonal, vertical and anti-diagonal by 0˚, 45˚, 90˚and

135˚respectively. Non-normalized frequencies of co-occurrence matrix as functions of distance, d and angle 0˚, 45˚, 90˚and 135˚can be represented respectively as

$$P_{0^\circ,d}(I_1,I_2)=\left|\left\{\begin{array}{l}\left[(k,l),(m,n)\right]\in \boldsymbol{D}:\\ k-m=0,\left|l-n\right|=d,\\ f(k,l)=I_1,f(m,n)=I_2\end{array}\right\}\right|$$

$$P_{45^\circ,d}(I_1,I_2)=\left|\left\{\begin{array}{l}\left[(k,l),(m,n)\right]\in \boldsymbol{D}:\\ (k-m=d,l-n=-d)\vee\\ (k-m=-d,l-n=d),\\ f(k,l)=I_1,f(m,n)=I_2\end{array}\right\}\right|$$

$$P_{90^\circ,d}(I_1,I_2)=\left|\left\{\begin{array}{l}\left[(k,l),(m,n)\right]\in \boldsymbol{D}:\\ k-m=d,\left|l-n\right|=0,\\ f(k,l)=I_1,f(m,n)=I_2\end{array}\right\}\right|$$

$$P_{135^\circ,d}(I_1,I_2)=\left|\left\{\begin{array}{l}\left[(k,l),(m,n)\right]\in \boldsymbol{D}:\\ (k-m=d,l-n=d)\vee\\ (k-m=-d,l-n=-d),\\ f(k,l)=I_1,f(m,n)=I_2\end{array}\right\}\right|$$

where $\left|\{\cdots\}\right|$ refers to cardinality of set, $f(k, l)$ is intensity at pixel position (k, l) in the image of order $(M\times N)$ and the order of matrix $\boldsymbol{D}$ is $(M\times N)\times(M\times N)$.

Using Co-occurrence matrix, features can be defined which quantifies coarseness, smoothness and texture-related information that have high discriminatory power. Among them, Angular Second Moment (ASM), Contrast, Correlation, Homogeneity and Entropy are few such measures which are given by:

$$\text{ASM} = \sum_{i,j} P(I_1, I_2)^2$$

$$\text{Contrast} = \sum_{I_1, I_2} |I_1 - I_2|^2 \log P(I_1, I_2)$$

$$\text{Correlation} = \sum_{I_1, I_2} \frac{(I_1 - \mu_1)(I_2 - \mu_2) P(I_1, I_2)}{\sigma_1 \sigma_2}$$

$$\text{Homogeneity} = \sum_{I_1, I_2} \frac{P(I_1, I_2)}{1 + |I_1 - I_2|^2}$$

$$\text{Entropy} = -\sum_{I_1, I_2} P(I_1, I_2) \log P(I_1, I_2)$$

ASM is a feature that measures the smoothness of the image. The less smooth the region is, the more uniformly distributed $P(I_1,I_2)$ and the lower will be the value of ASM. Contrast is a measure of local level variations which takes high values for image of high contrast. Correlation is a measure of correlation between pixels in two different directions. Homogeneity is a measure that takes high values for low-contrast images. Entropy is a measure of randomness and takes low values for smooth images. Together

all these features provide high discriminative power to distinguish two different kind of images. All features are functions of the distance dand the orientation θ. Thus, if an image is rotated, the values of the features will be different. In practice, for each d the resulting values for the four directions are averaged out. This will generate features that will be rotations invariant.

2.3.1.2 LBP Methods

The other important category of statistical methods is Local Binary Pattern (LBP) based approaches. In a new LBP method has been proposed which tries to incorporate spectral features into LBP method. Therefore, LBP will be more robust and powerful to invariant texture analysis in this case. Different types of this method have been proposed for texture analysis of biomedical applications and find a great attention in CAD systems (Ahmadvand et al., 2015b).

2.3.1.3 Model Based Approaches:

Some researchers have tried to model contextual, textural and spatial properties of images and then texture features can be extracted by incorporating these features during image analysis. The main categories of model based methods which have been considered for this aim are Markov models. These methods have different types including the Gaussian Markov random fields and Gibbs random fields. In fact, Markov random field method is an optimization method which defines an energy function on a label field and the goal is to minimize the energy function. This energy function must be defined in a way that textural features and also spatial relationships of neighborhood pixels to be considered. Methods based on auto-regressive and Hidden Markov Model have been proposed for texture

Classification and have had good results in this field(Ahmadvand and Kabiri, 2016).

2.3.1.4 Filter Banks Based Methods:

The other important groups of texture analysis methods which have been considered in biomedical image analysis applications are filter bank based methods. The filter bank methods consist of three main sub-categories including the frequency, spatial and spatial-frequency approaches. Frequency filter banks mainly use Fourier transform and discrete cosine transform for extraction of features and try to extract the texture feature in frequency domain. On the other hand, spatial methods just apply filter banks on spatial domain of textures and then extract the texture features from the image(Leung and Malik, 2001).

2.3.1.5Spatial filter banks and frequency analysis based approaches:

Spatial filter banks have long history for biomedical feature extraction. These methods are containing of two important groups such as smoothing filters like Gaussian filters and sharpening filters like Laplacian and Sobel filters. However, recently, different authors inspired from the visual cortex, try to use a bank of oriented spatial Filters in different scales for modeling of texture images(Gevaa et al., 2016).

2.3.1.6 Spatial-frequency based methods:

Frequency analysis just decomposes each signal into frequency components of the signal and completely ignores the spatial domain. Moreover, spatial filters just consider the spatial information; therefore, these two groups of methods intrinsically have limitation for analysis of textures(Bhateja et al.,

2015).These shortcomings could be solved if both the spatial and spectral information considered because appropriate analysis of real world images needs both information. Spatial-frequency methods include a range of filter banks which wavelet transform and Gabor filter are among the most important ones. In most feature based methods such as pyramid-structured wavelet transforms and tree-structured wavelet transform (TSWT), texture features are extracted by some features in different resolution and channels, two way for combination of DWT method with spatial filter banks is proposed and try to incorporate spectral information in multi-resolution analysis methods like DWT for extraction of invariant features. DWT based methods are very important for biomedical image analysis. The other important multi resolution based methods are Gabor filters and Gabor wavelets. According to the ability of Gabor filters for invariant texture analysis these methods have provided good results in biomedical image analysis applications(Zou et al., 2016).

2.4 Basics CT imaging:

2.4.1 Principles of Helical CT Scanners

The development of helical or spiral CT around 1990 was a truly revolutionary advancement in CT scanning that finally allowed true 3D image acquisition within a single breath hold. The technique involves the continuous acquisition of projection data through a 3D volume of tissue by continuous rotation of the x-ray tube and detectors and simultaneous translation of the patient through the gantry opening (Kalender, et al, 1990). Three technological developments were required: slip-ring gantry designs,

very high power x-ray tubes, and interpolation algorithms to handle the non-coplanar projection data (Beck, 1996).

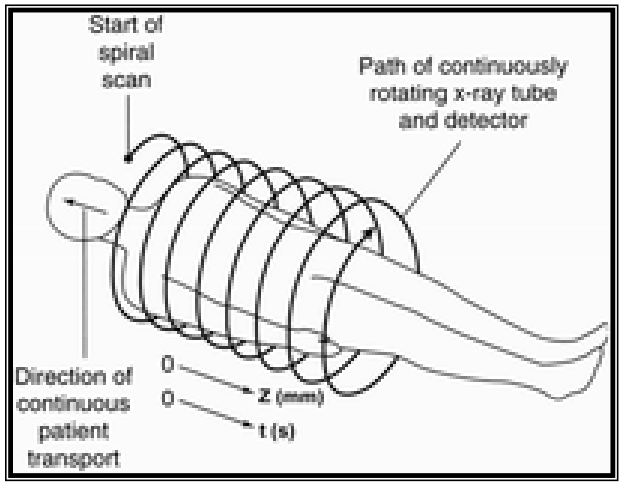

Figure 2.4: Principles of helical CT. As the patient is transported through the gantry, the x-ray tube traces a spiral or helical path around the patient, acquiring data as it rotates. t = time in seconds (Mahesh, 2002).

2.4 .2 Slip-Ring Technology

Slip rings are electromechanical devices consisting of circular electrical conductive rings and brushes that transmit electrical energy across a moving interface. All power and control signals from the stationary parts of the scanner system are communicated to the rotating frame through the slip ring. The slip-ring design consists of sets of parallel conductive rings concentric to the gantry axis that connect to the tube, detectors, and control circuits by sliding contactors. These sliding contactors allow the scan frame to rotate continuously with no need to stop between rotations to rewind system cables (Brunnettet al., 1994). This engineering advancement resulted initially from a desire to reduce inter scan delay and improve throughput. However,

reduced interscan delay increased the thermal demands on the x-ray tube; hence, tubes with much higher thermal capacities were required to withstand continuous operation over multiple rotations. (Mahesh, 2002)

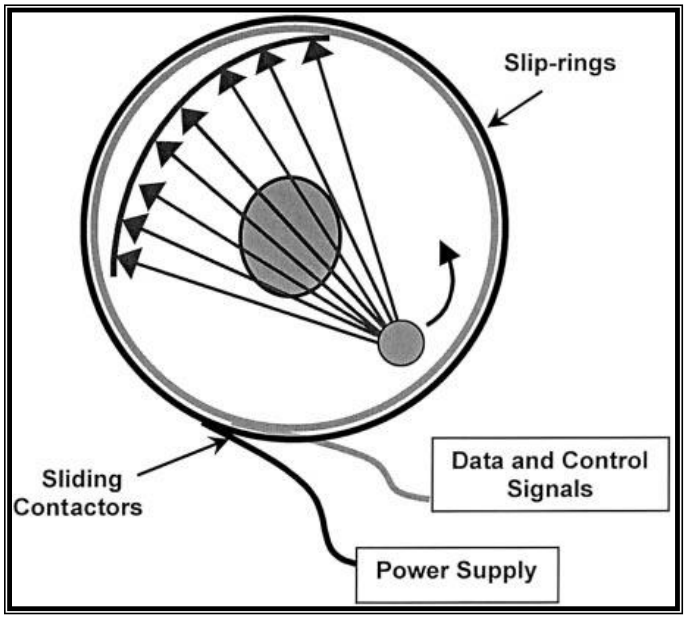

Figure 2.5: Diagram of the slip-ring configuration. Sliding contactors permit continuous rotation of the x-ray tube and detectors while maintaining electrical contact with stationary components.

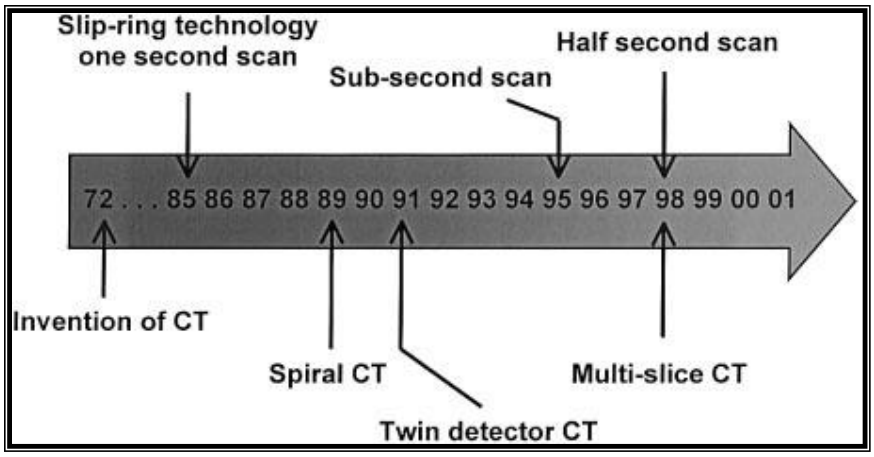

Figure 2.6: Time line of the key technological developments in CT

2.4.3 Capabilities of Single-Row Detector Helical CT

With the advent of helical CT, considerable progress was made on the road toward 3D radiography. An example of a 3D reconstruction from single-row detector helical scanning is shown in Fig (2.9).Complete organs could be scanned in about 30–40 seconds; artifacts due to patient motion and tissue misregistration due to involuntary motion were virtually eliminated. It became possible to generate sections in any arbitrary plane through the scanned volume. Significant improvements in z-axis resolution were achieved due to improved sampling, since sections could be reconstructed at fine intervals less than the section width along the z axis. Near-isotropic resolution could be obtained with the thinnest (∼1 mm) section widths at a pitch of 1, but this could be done only over relatively short lengths due to tube and breath-hold limitations (Kalender 1995), (Levy, 1995). Higher-power tubes capable of longer continuous operation coupled with faster rotation speeds could scan greater lengths with higher resolution. The practical limit on such brute force approaches, however, became the length

of time a sick patient could reliably suspend breathing. This turns out to be no more than 30 seconds. Even though the z-axis resolution for helical CT images far exceeds that of conventional CT images, the type of interpolation algorithm and the pitch still affect the overall image quality. The section sensitivity profiles of helical CT images are different compared with those of conventional CT images, which are influenced by the type of interpolation algorithm and the selected pitch.

2.4.4 Multiple-Row Detector Helical CT

Continued scanner development on the road to a 3D radiograph called for further progress, but single-row detector helical scanners had reached their limits. An obvious improvement would be to make more efficient use of the x rays that are produced by the tube while improving z-axis spatial resolution; this led to the development of multiple-row detector arrays. The principal difference between single- and multiple-row detector helical scanners is illustrated in Figure (2.7). The basic idea actually dates to the very first EMI Mark I scanner, which had two parallel detectors and acquired two sections simultaneously.

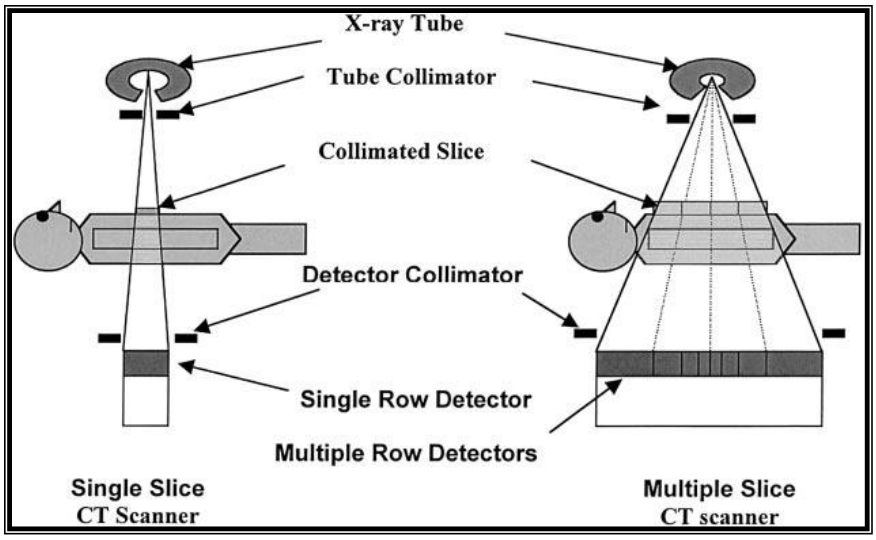

Figure 2.7: Diagram shows the difference between single-row detector and multiple-row detector CT designs. The multiple-row detector array shown is asymmetrical and represents that of one particular manufacturer.

The first helical scanner to use this idea, the CT Twin was launched in 1992. (Mahesh, 2002).This design was so superior to single-row detector designs that all scanner manufacturers went back to the drawing board. By late 1998, all major CT manufacturers launched multiple-row detector CT scanners capable of acquiring at least four sections per rotation. The arrangement of detectors along the z axis and the widths of the available sections vary between the systems. Fig (2.8) illustrates different multiple-row detector array configurations from several manufacturers.

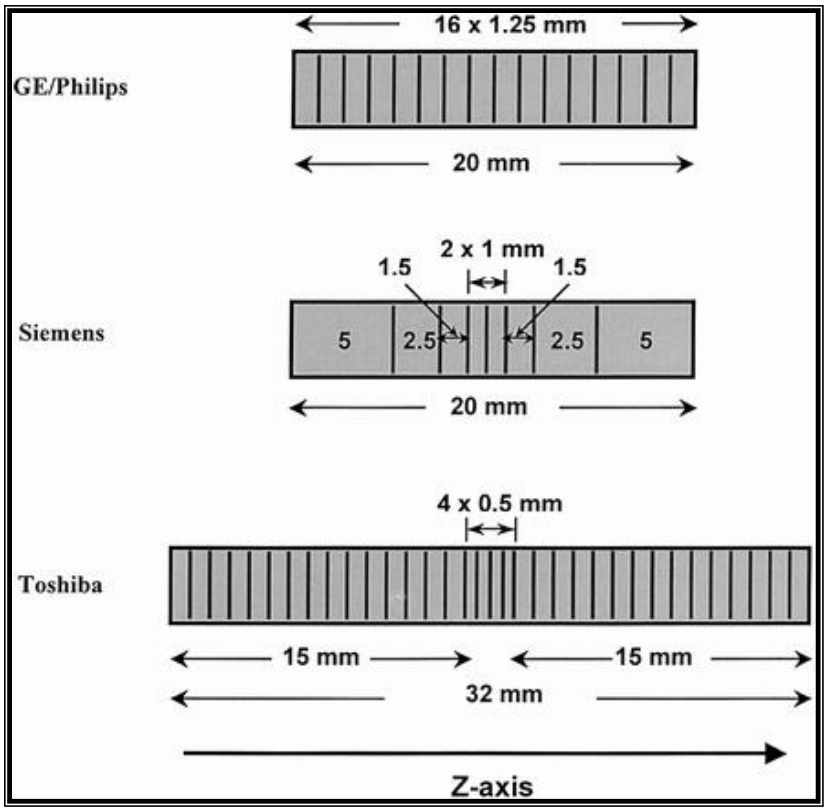

Figure 2.8: Various detector array designs used in multiple-row detector CT scanners.

In single-row detector helical CT designs, scan volume can be increased with an increased pitch at the expense of poorer z-axis resolution, whereas z-axis resolution can be preserved in multiple-row detector designs. For example, if a 10-mm collimation were divided into four 2.5-mm detectors, the same scan length could be obtained in the same time but with a z-axis resolution improved from 10 mm to 2.5 mm. In another example, a multiple-row detector scanner with four 5-mm detectors and a beam width of 20 mm reduces the scan time by a factor of 4–15 seconds for the same z-axis resolution (Mahesh, 2002). By increasing the number of CT scanner detector rows, data acquisition capability dramatically increases while greatly

improving the efficiency of x-ray tubes. Further developments in scanner rotational speeds and tube outputs have made isotropic resolution a practical possibility with even better improvements on the horizon. Current multiple-row detector scanners can scan large 40-cm volume lengths in less than 30 seconds with near-isotropic resolution and image quality that could not be envisioned at the time of Hounsfield's invention.

MDCT systems are CT scanners with a detector array consisting of more than a single row of detectors. The "multi-detector-row" nature of MDCT scanners refers to the use of multiple detector arrays (rows) in the longitudinal direction (that is, along the length of the patient lying on the patient table). MDCT scanners utilize third generation CT geometry in which the arc of detectors and the x-ray tube rotate together. All MDCT scanners use a slip-ring gantry, allowing helical acquisition at rotation speeds as fast as 0.33 second for a full rotation of 360 degrees of the X-ray tube around the patient. A scanner with two rows of detectors (Mahesh, 2002) had already been on the market since 1992 and MDCT scanners with four detector rows were introduced in 1998 by several manufacturers. The primary advantage of these scanners is the ability to scan more than one slice simultaneously and hence more efficiently use the radiation delivered from the X-ray tube (Fig.2.11). The time required to scan a certain volume could thus be reduced considerably.

The number of slices, or data channels, acquired per axial rotation continues to increase, with 64-detector systems now common (Flohr et al., 2005a; Flohr et al., 2005b). It is likely that in the coming years even larger arrays of detectors having longitudinal coverage per rotation > 4 cm will be commercially available. Preliminary results from a 256-detector scanner

(12.8 cm longitudinal coverage at the center of rotation) have already been published (Mori et al., 2004). Further, an MDCT system with two x-ray sources is now commercially available, signaling continued evolution of CT technology and applications (Flohr et al., 2006).

MDCT scanners can also be used to cover a specific anatomic volume with thinner slices. This considerably improves the spatial resolution in the longitudinal direction without the drawback of extended scan times. Improved resolution in the longitudinal direction is of great value in multiplanar reformatting (MPR, perpendicular or oblique to the trans axial plane) and in 3-dimensional (3D) representations. Spiral scanning is the most common scan acquisition mode in MDCT, since the total scan time can be reduced most efficiently by continuous data acquisition and overlapping data sets and this allows improved multi-planar reconstruction (MPR) and 3D image quality to be reconstructed without additional radiation dose to the patient.

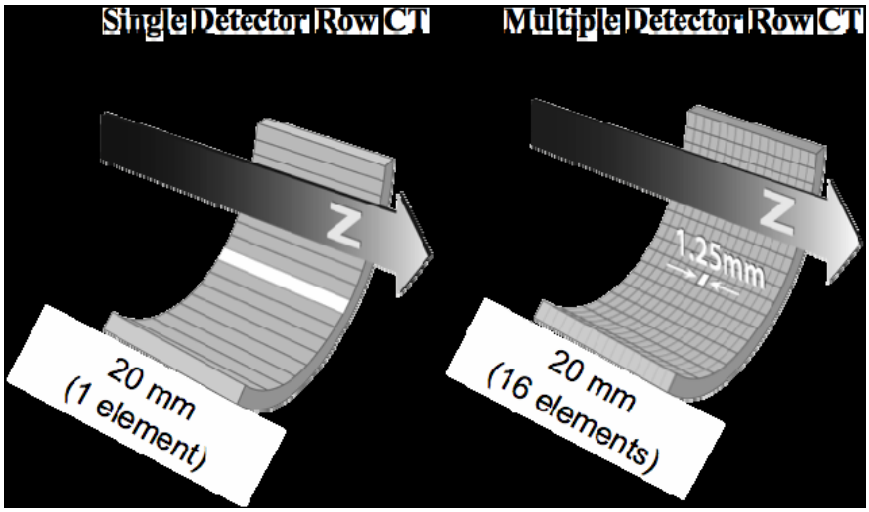

Figure 2.9: single CT detector versus Multi slice CT detector.

2.4.5 CT imaging protocol

The technique used in CT-scanners share most of its characteristics with conventional X-ray imaging, and the prime differences are seen in projection, detection and acquisition as presented in Figure 2.10 below.

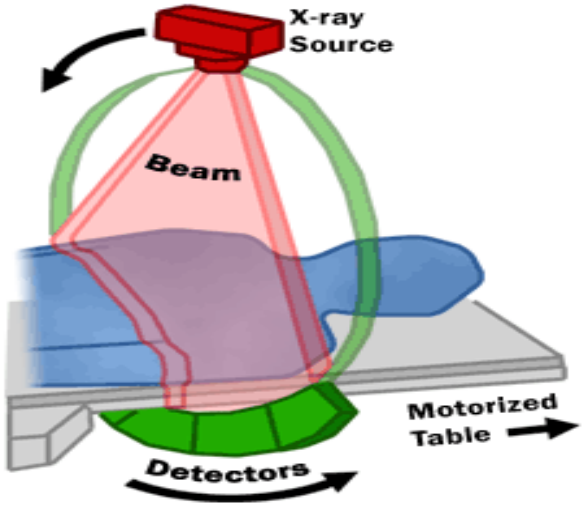

Figure 2.10 Simple overview of a third generation CT-imaging system

2.4.6 Parameters

In order to properly calculate and compare doses, it is imperative to have a standardized nomenclature to ensure that all data is comparative (Kalra, M. K ,et al 2006). Without this, it will be difficult to reproduce measurements, and to develop consistent protocols. When performing a CT examination, a number of parameters are defined by the operator. The thesis will cover the parameters deemed important for correct, uniform dosimetry: tube current, tube voltage, rotation time, total scan length, slice thickness and pitch.

Automatic exposure control (AEC) and iterative reconstruction will be briefly covered, as their impact on dose and image quality is more of a qualitative influence than a quantitative one.

2.4.6.1 Tube current

The tube current [mA] influences the number of photons exiting the X-ray tube, as it determines the number of electrons leaving the cathode. The tube current is directly proportional to radiation dose, and as such is a prime parameter in adjusting the dose. Instead of tube current is sometimes used the tube-current-time-product [mAs], which is the tube current multiplied with the scan time.

2.4.6.2 Tube Voltage

The tube voltage [kV] determines the voltage across the anode and cathode of the X-ray tube, and therefore the acceleration of the electrodes across the interior vacuum. This determines the kinetic energy of the electrodes when they reach the anode, and therefore the number of interactions they can initiate before being absorbed. As a consequence, an increase in tube voltage will increase the dose, all other factors kept constant; however, the increase is not directly proportional as was the case with current. Voltage determines the energy of the electrons, and therefore the energy distribution of the incident X-rays. It is rarely adjusted from the customary value of 120 kV. Certain examinations use a different voltage, but seldom outside the range of 80 to 140 kV (Kalra, M. K ,et al 2006).

2.4.6.3 Rotation Time

The rotation time of the gantry [s] has decreased greatly over the last few decades, with modern scanners having a rotation time in the area of 0.4 seconds. The main consequence of the decreased rotation time is an increase

in the noise and a reduction in absorbed dose. To avoid the noise, it is customary to increase the tube current accordingly (M. K., Maher,et al 2004).

2.4.6.4 Total Scan Length

It is apparent that the total scan length [cm] influence the absorbed dose, as an increase in scan length will expose a larger part of the patient to radiation. Therefore, it is imperative that scan length is to be limited to cover just the diagnostically relevant part of the patient; otherwise, an unnecessary increase in dose will be seen (ICRP, 2000). This is relatively easy with SSCT; however, the situation is more complicated for MSCT. At the initiation of the scan, the X-ray tube will be activated the moment the first row of detectors reach the diagnostic area. The X-ray beam will irradiate the entire detector-array, but only the first row of detectors will be acquiring image data. The remaining detector rows will not acquire data, but the area will still be irradiated. This is called over scan, and a small degree of over scan is required for correct reconstruction. As the table moves, more rows of detectors are entering the diagnostic area, contributing to the image. At the reverse end of the patient, the same scenario occurs, and a noteworthy part of the dose is absorbed in the patient outside the diagnostic area (M. K., Maher, et al 2004).

2.4.6.5 Slice Thickness

In SSCT, with only a single row of detectors, the slice thickness [cm] is determined by simple collimation. The maximum slice thickness is limited by the width of the individual detector element (typically 10 mm (M. K., Maher, et al 2004)), and by collimating the beam, this thickness can be decreased. In other words, the width of the beam is equal to slice thickness. In MSCT, the width of each individual detector element in the longitudinal

direction determines the minimum slice thickness, and by merging multiple adjacent detector elements during detection, one can increase the slice thickness. This has a significant impact on image quality, as thin slices have better spatial resolution compared to thick slices, but lower SNR. To address the decrease in SNR, it is necessary to increase for instance the tube current, resulting in a significant increase in dose to the patient (Kalender,et al,2005).

2.4.6.6 Pitch

With the prevalence of helical MSCT, it is necessary to incorporate the incremental movement of the table, in relation to the irradiated area. This is defined as pitch, being the increment of the table per rotation, divided by the width of the beam. In Figure 2.13 below, a 4-slice MSCT is rotated twice around the patient, resulting in the acquisition of eight slices in pairs of two (indicated by color). The slices are in reality at an incline, as the patient is moving during exposure.

pitch = table feed per rotation/collimation

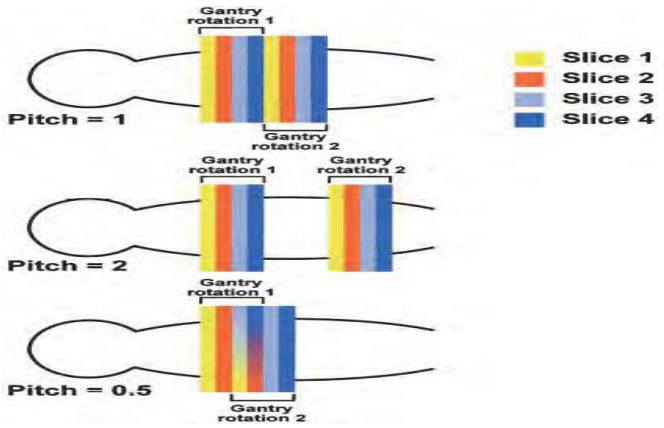

Figure 2.11the effect of pitch on irradiated area, with overlap for pitch < 1 (23

2.4.6.7 Automatic Exposure Control:

Technological advances lead to the development of a technique where the tube current is modulated in real-time, in order to minimize the dose while retaining image quality. This technique, Automatic Exposure Control (AEC) varies the tube current during exposure. The variance is relative to patient thickness, optimized to achieve dose distribution defined by a desirable image quality. It is possible to achieve a significant reduction in dose based on which type of AEC is used: either the exposure varies within a single slice, i.e. in the image plane of the slice, or it is modulated in the longitudinal direction of the patient. It is also possible to combine these two types of AEC.

2.5 Previous studies:

The study conducted by (Meredith et.al, 2011) Single-slice measurements were obtained in 92 participants (mean age 60 years, 49% women, median renal sinus fat 0.43 cm2). Intra- and inter-reader intra-class correlation coefficients were 0.93 and 0.86, respectively. Single-slice renal sinus fat was correlated with body mass index ($r = 0.35$, $p = 0.0006$), waist circumference ($r = 0.31$, $p = 0.003$), and abdominal visceral fat ($r = 0.48$, $p < 0.0001$). Similar correlations were observed for volumetric renal sinus fat in the right kidney.

Chapter Three

Materials and Methods

3.1 Materials:

3.1.1 Subjects:

This was a cross sectional descriptive study done to evaluate the renal sinus fat. 50 images enrolled in the study. The study conducted at radiology department in Royal Care hospital.

3.1.2 Machine Used

The machine used was CT scan 64 slice manufactured by Toshiba.

3.2 Methods:

3.2.1 Imaging Technique Used

All patients scanned with the following imaging parameters:

Kvp(120-140), mAs (140-160).

Slice thickness: 5 mm

Breath hold: yes

Intravenous Contrast: None

Patient position: Supine head first, the arms were raised and placed behind the head.

Start location and end: From Diaphragm to pubis.

3.2.2 Image analysis:

After that CT images were stored in computer disk were viewed by the Radiant, Ant DICOM in computer to selected the axial images that suit the criteria of research population then uploaded into the computer based software Interactive Data Language (IDL) where the DICOM image

converted to TIFF format to suit IDL platform. Then the image were read by IDL in TIFF format and the user clicks on areas represents the renal cortex, renal sinus fat and psoas muscle fat area in case of test group; in these areas a window 3×3 pixel were generated and textural feature for the classes center were generated. These textural features includes FOS; (coefficient of variation, stander deviation, variance, signal, energy, and entropy) were used. These features were assigned as classification center using the Euclidian distances to classify the whole image. The algorithm scans the whole image using a window; 3×3 pixels and computes the above mentioned textural features and then computes the distance (the Euclidean distance) between the calculated features during the scanning and the class's centers and assigns the window to the class with the lowest distance. Then the window interlaced one pixel and the same processes started over again till the entire image were classified and classification maps were generated. After all images were classified the data concerning the renal cortex, renal sinus fat and psoas muscle fat entered into SPSS with its classes to generate a classification score using stepwise linear discriminate analysis; to select the most discriminate features that can be used in the classification of renal sinus fat in CT images. Where scatter plot using discriminate function were generated as well as classification accuracy and linear discriminate function equations to classify renal sinus fat into the previous classes without segmentation process for unseen images in routine work.

3.2.3 Statistical analysis:

All statistical analyses were performed using the SPSS 19.0 for Windows. All parametric results were expressed as mean ± standard deviation. Differences were considered significant if *p* values were less than 0.05.

Chapter Four

Results

Table 4.1 Classification Results[a,c]						
		Classes	Predicted Group Membership			Total
			Renal sinus fat	Kidney tissue	Abdominal fat	
Original	Count	Renal sinus fat	228	1	31	260
		Kidney tissue	0	200	0	200
		Abdominal fat	13	0	205	218
	%	Renal sinus fat	87.7	.4	11.9	100.0
		Kidney tissue	.0	100.0	.0	100.0
		Abdominal fat	6.0	.0	94.0	100.0

93.4% of original grouped cases correctly classified. Overall classification accuracy =93.4%. Sensitivity of renal sinus, kidney tissue and abdominal fat =87.7%, 100%, and 94.0% respectively.

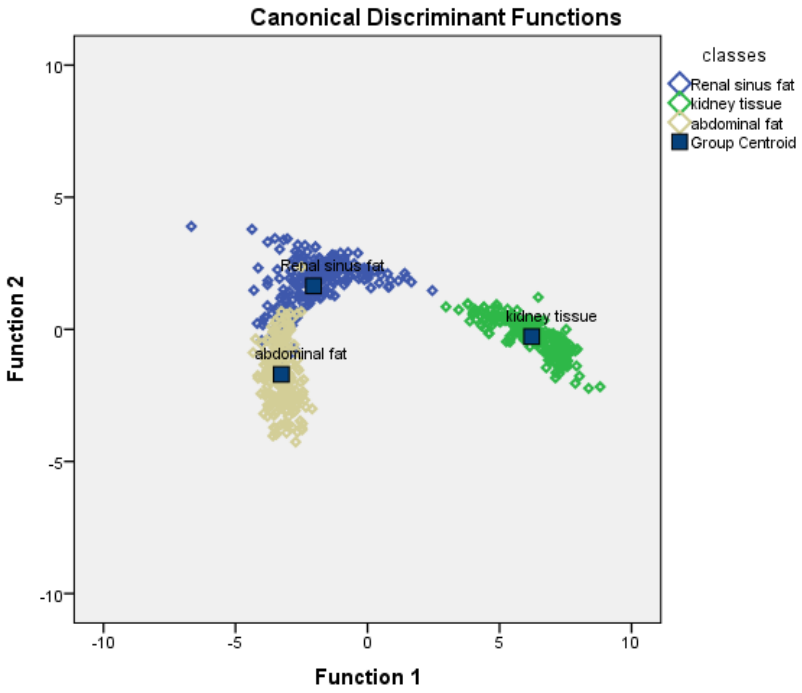

Figure 4.1 classification Map that created using linear discriminant analysis, function to predicted overall accuracy showed 94.4%

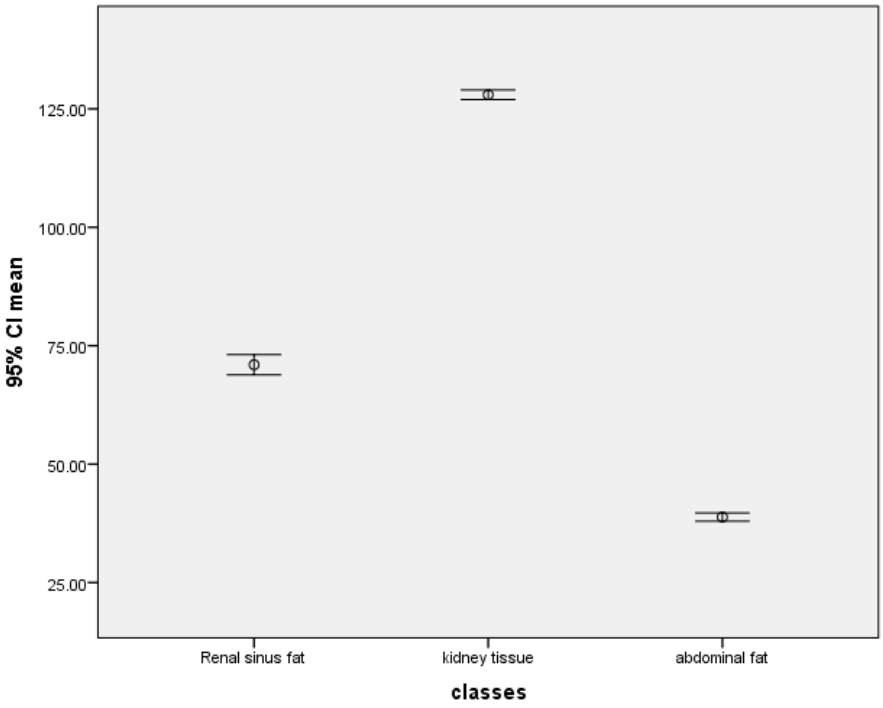

Figure 4.2 Error bar plot show the discriminate power of the mean textural feature distribution for the selected classes on CT images.

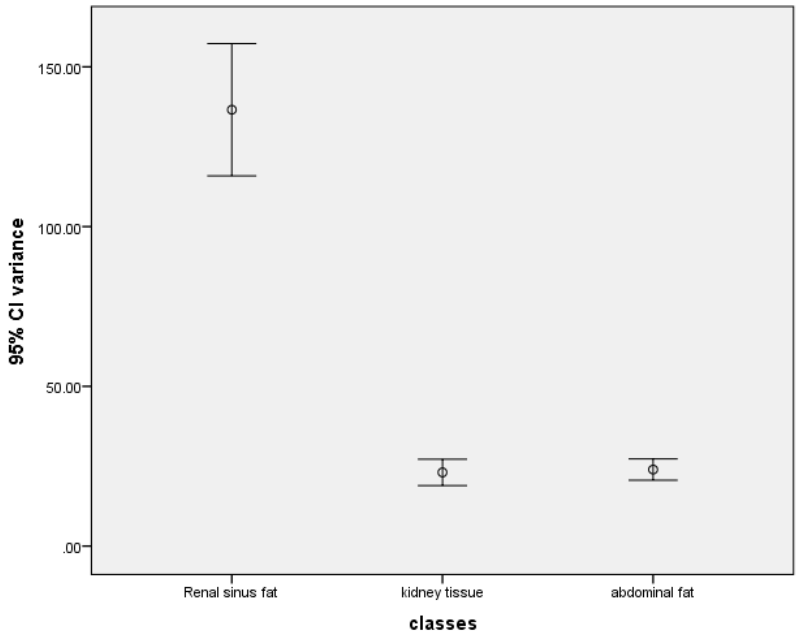

Figure 4.3Error bar plot show the discriminate power of the variance textural feature distribution for the selected classes on CT images.

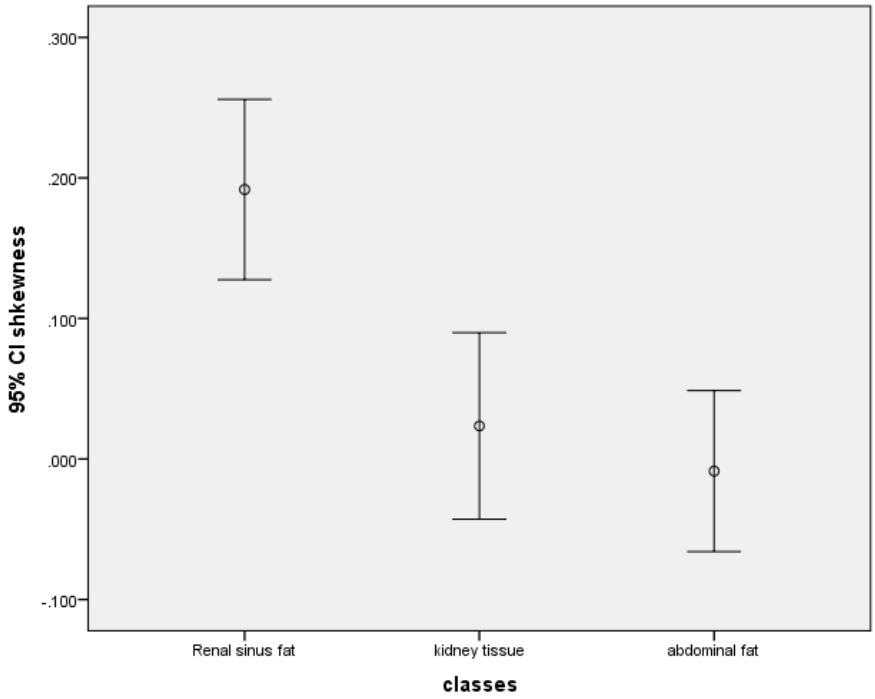

Figure 4.4 Error bar plot show the discriminate power of the skewness textural feature distribution for the selected classes on CT images.

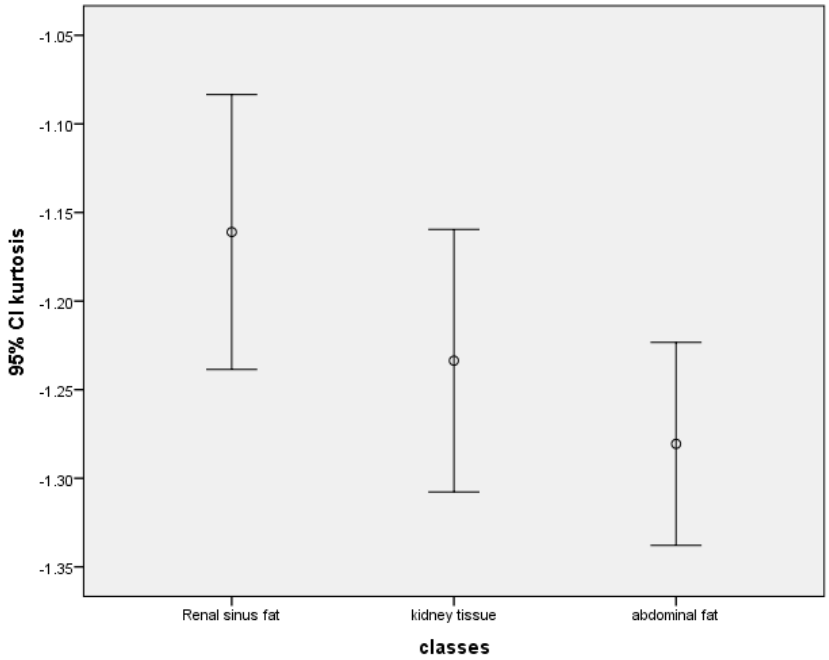

Figure 4.5 Error bar plot show the discriminate power of the Kurtosis textural feature distribution for the selected classes on CT images.

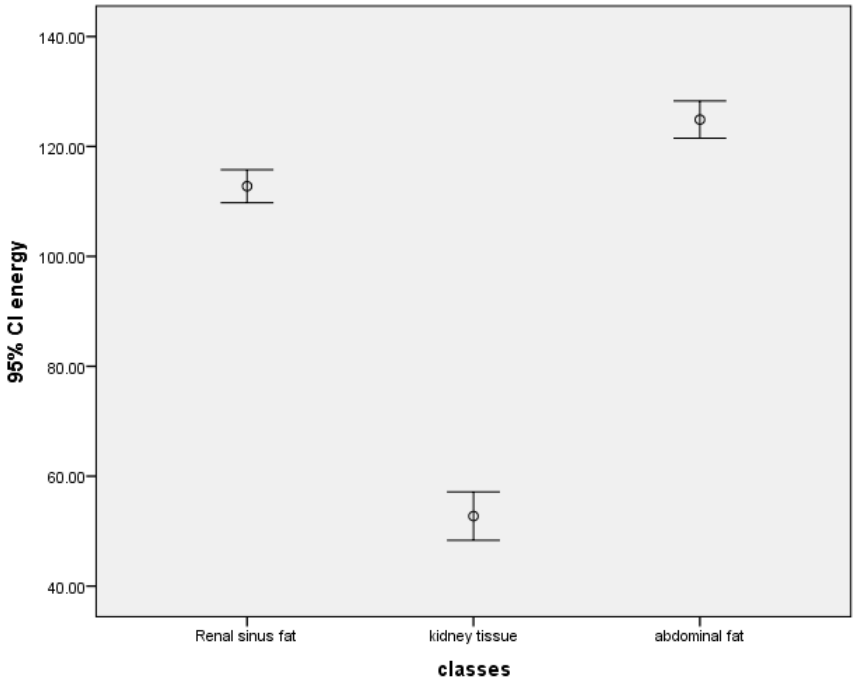

Figure 4.6 Error bar plot show the discriminate power of the energy textural feature distribution for the selected classes on CT images.

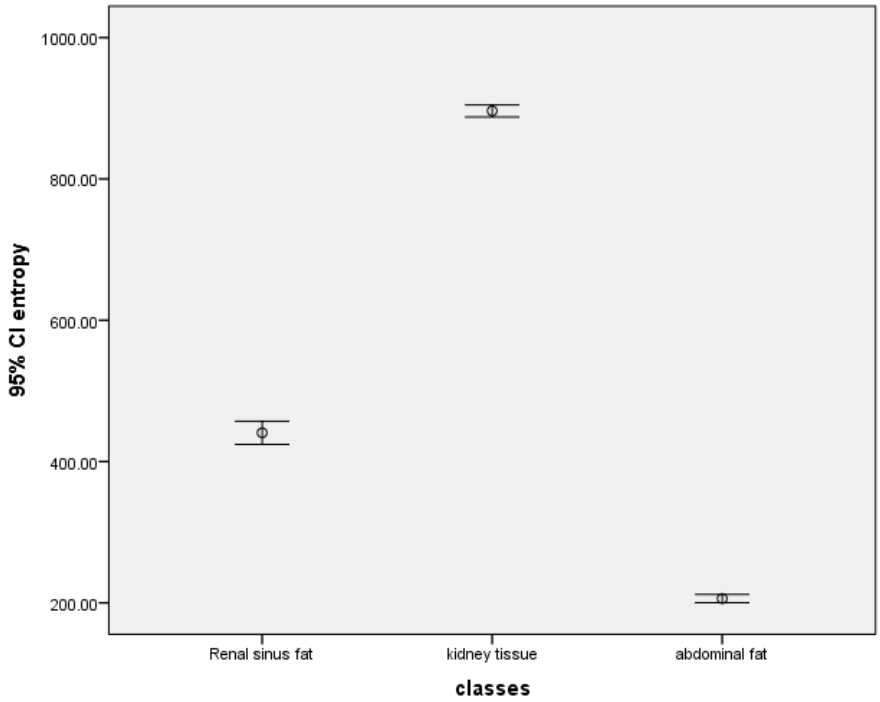

Figure 4.7 Error bar plot show the discriminate power of the mean textural feature distribution for the selected classes on CT images.

Table 4.2 Classification Function Coefficients			
	classes		
	Renal sinus fat	kidney tissue	abdominal fat
Mean	32.785	24.995	29.236
Variance	.045	-.012	.042
Skewness	4.060	4.966	1.997
Energy	.225	.103	.238
Entropy	-4.254	-3.151	-3.818
(Constant)	-243.237	-191.133	-190.525
Fisher's linear discriminant functions			

Renal sinus fat= (mean*32.785) + (variance*0.045) + (skewness*4.06) + (energy*0.225) + (entropy*-4.254)-243.237

Chapter Five

Discussion, Conclusion and Recommendations

5.1Discussion:

CT scan obtained from imaging sequences which aim to differentiate between different renal tissues according to its intensities, this study was conducted using axial CT image to characterize the renal sinus fat. As shown in Figure 1, the classification Map that created using linear discriminant analysis functions where the three different tissue classes of renal cortex, renal sinus fat and abdominal fat were clearly separated according to calculated texture at $P<0.05$, and CL=95%. Table (1): Showed the classification accuracy result using linear discriminant function, in which 93.4% of original grouped cases correctly classified. Overall classification accuracy = 93.4%. Sensitivity of renal sinus, kidney tissue and abdominal fat = 87.7%, 100%, and 94.0% respectively. This result for 3x3 windows generated using step-wise technique to select the most significant features that can be used for purpose of renal sinus fat characterization which are: mean variance, energy and entropy from first order statistics. The result also showed that the result of the classification of the renal sinus tissue tissues were very different from result of the tissues.

Although by definition, visual analysis of the CT image appears with abdominal fat, the texture parameter maps validate the fact that there are indeed subtle differences, but these differences surface only upon numerical processing of the images. These maps were obtained by selecting a small neighborhood around each image pixel, computing the texture parameter for that neighborhood, and then attributing the value of this parameter to the pixel. This was done for all renal pixels and not just in the region of interest.

Nevertheless, these maps give an idea about the texture variation in the kidney and its surrounding tissues, and they “visually” show that there are, indeed, texture differences of the renal sinus and extension over the abdominal fat.

In respect to the applied features the mean, SD, energy and entropy on CT images can differentiate between renal sinus fat and rest of the tissue successfully and the best feature is the mean followed by energy, then entropy and the least is SD.

Texture analysis depending on the relative attenuation coefficient of tissues i.e. the CT No in HU could serves the diagnostic field and overcoming the visual diagnosis that comes with different interpretation and also would have promising future to avoid invasive technique if the base line for individual tissues being determined and algorithmic aided computer have been applied.

5.2 Conclusion:

The study concluded that CT is first choice compared with other modality due to many advantages it have such as need short time for procedure and accurately identifies the renal abnormalities such as stone and obstruction.
Renal sinus fat accumulation can be measured using computed tomography. In respect to the applied features the mean, SD, energy and entropy on CT images can differentiate between renal sinus fat and rest of the tissue successfully and the best feature is the mean followed by energy, then entropy and the least is SD.

Texture analysis depending on the relative attenuation coefficient of tissues i.e. the CT No in HU could serves the diagnostic field and overcoming the visual diagnosis that comes with different interpretation and also would have promising future to avoid invasive technique if the base line for individual tissues being determined and algorithmic aided computer have been applied.

5.3 Recommendations

The study ends with in the following recommendation:

- Further studies in evaluation renal dimension with larger sample of population for more accurate results. Also renal sinus fat volume should be measured after classification.
- Further studies must achieve bearing in mind the body weight.
- Further studies must achieve with the effect the age and gender.

References:

AHMADVAND, A., AHMADVAND, R., HAJIALI, M. T. & MOSAVI, M. R. A novel CMC based method for MR! brain image segmentation. Knowledge-Based Engineering and Innovation (KBEI), 2015 2nd International Conference on, 2015a. IEEE, 158-163.

AHMADVAND, A., AHMADVAND, R., HAJIALI, M. T. & MOSAVI, M. R. A novel LBP method for invariant texture classification. Knowledge-Based Engineering and Innovation (KBEI), 2015 2nd International Conference on, 2015b. IEEE, 152-157.

AHMADVAND, A. & DALIRI, M. R. 2015. Improving the runtime of MRF based method for MRI brain segmentation. *Applied Mathematics and Computation,* 256**,** 808-818.

AHMADVAND, A. & KABIRI, P. 2016. Multispectral MRI image segmentation using Markov random field model. *Signal, Image and Video Processing,* 10**,** 251-258.

BHATEJA, V., PATEL, H., KRISHN, A., SAHU, A. & LAY-EKUAKILLE, A. 2015. Multimodal medical image sensor fusion framework using cascade of wavelet and contourlet transform domains. *IEEE Sensors Journal,* 15**,** 6783-6790.

DEPEURSINGE, A., FONCUBIERTA-RODRIGUEZ, A., VAN DE VILLE, D. & MÜLLER, H. 2014. Three-dimensional solid texture analysis in biomedical imaging: Review and opportunities. *Med Image Anal,* 18**,** 176-196.

DIETRICH, R. B. & KANGARLOO, H. 1986. Kidneys in infants and children: evaluation with MR. *Radiology,* 159**,** 215-21.

DWYER, T. M., MIZELLE, H. L., COCKRELL, K. & BUHNER, P. 1995. Renal sinus lipomatosis and body composition in hypertensive, obese rabbits. *Int J Obes Relat Metab Disord,* 19**,** 869-74.

GEVAA, O., LIEBERMANC, S., KONENC, E. & GREENSPANB, H. Localized Fisher vector representation for pathology detection in chest radiographs. SPIE Medical Imaging, 2016. International Society for Optics and Photonics, 97850D-97850D-7.

HARALICK, R. M. & SHANMUGAM, K. 1973. Textural features for image classification. *IEEE Transactions on systems, man, and cybernetics***,** 610-621.

KARAHALIOU, A., SKIADOPOULOS, S., BONIATIS, I., SAKELLAROPOULOS, P., LIKAKI, E., PANAYIOTAKIS, G. & COSTARIDOU, L. 2007. Texture analysis of tissue surrounding microcalcifications on mammograms for breast cancer diagnosis. *Br J Radiol,* 80**,** 648-656.

LEUNG, T. & MALIK, J. 2001. Representing and recognizing the visual appearance of materials using three-dimensional textons. *International journal of computer vision,* 43**,** 29-44.

MONTANI, J. P., CARROLL, J. F., DWYER, T. M., ANTIC, V., YANG, Z. & DULLOO, A. G. 2004. Ectopic fat storage in heart, blood vessels and kidneys in the pathogenesis of cardiovascular diseases. *Int J Obes Relat Metab Disord,* 28 Suppl 4**,** S58-65.

MURAKAMI, Y., NAGATANI, Y., TAKAHASHI, M., IKEDA, M., MIYAZAWA, I., MORINO, K., OHKUBO, T., MAEGAWA, H., NITTA, N., SAKAI, H., NOTA, H., USHIO, N. & MURATA, K. 2016. Data set for renal sinus fat volume and visceral adipose tissue volume on computed tomography. *Data Brief,* 7**,** 1658-64.

OJALA, T., VALKEALAHTI, K., OJA, E. & PIETIKÄINEN, M. 2001. Texture discrimination with multidimensional distributions of signed gray-level differences. *Pattern Recognition*, 34**,** 727-739.

PATTON, K. T. 2015. *Anatomy and physiology*, Elsevier Health Sciences.

SOKHI, H. K., MOK, W. Y. & PATEL, U. 2015. Stage T3a renal cell carcinoma: staging accuracy of CT for sinus fat, perinephric fat or renal vein invasion. *Br J Radiol*, 88**,** 20140504.

TARZAMNI, M. K., NEZAMI, N., ZOMORRODI, A., FATHI-NOROOZLOU, S., PIRI, R., NAGHAVI-BEHZAD, M., MOJADIDI, M. K. & BIJAN, B. 2016. Renal Collecting System Anatomy in Living Kidney Donors by Computed Tomographic Urography: Protocol Accuracy Compared to Intravenous Pyelographic and Surgical Findings. *J Clin Imaging Sci*, 6**,** 1.

VORA, A. N., STANISLAWSKI, M., GRUNWALD, G. K., PLOMONDON, M. E., RUMSFELD, J. S., MADDOX, T. M., VIDOVICH, M. I., WOODY, W., NALLAMOTHU, B. K., GURM, H. S. & RAO, S. V. 2017. Association Between Chronic Kidney Disease and Rates of Transfusion and Progression to End-Stage Renal Disease in Patients Undergoing Transradial Versus Transfemoral Cardiac Catheterization-An Analysis From the Veterans Affairs Clinical Assessment Reporting and Tracking (CART) Program. *J Am Heart Assoc*, 6.

ZOU, Z., YANG, J., MEGALOOIKONOMOU, V., JENNANE, R., CHENG, E. & LING, H. Trabecular bone texture classification using wavelet leaders. SPIE Medical Imaging, 2016. International Society for Optics and Photonics, 97880E-97880E-6.